Materials Chemistry and Physics xxx (xxxx) 125464

Contents lists available at ScienceDirect

Materials Chemistry and Physics

journal homepage: www.elsevier.com/locate/matchemphys

Insights into photocatalytic mechanism for the rational design of p-n heterojunction by decorating mesoporous SnS_2 over $ZnFe_2O_4$ nanocomposite for accelerated visible light photocatalysis

C. Akshhayya [a], Mohammad K. Okla [b], Ajith M. Thomas [c], Abdullah A. AL-ghamdi [b], Mostafa A. Abdel-Maksoud [d], Bander Almunqedhi [b], Hamada AbdElgawad [e], Lija L. Raju [f], S. Sudheer Khan [a], *

[a] *Nanobiotechnology Laboratory, Department of Biotechnology, Bannari Amman Institute of Technology, Sathyamangalam, Tamil Nadu, India*
[b] *Botany and Microbiology Department, College of Science, King Saud University, P.O. Box 2455, Riyadh, 11451, Saudi Arabia*
[c] *Department of Botany and Biotechnology, St Xavier's College, Thumba, Thiruvananthapuram, India*
[d] *Zoology Department, College of Science, King Saud University, P.O. Box 2455, Riyadh, 11451, Saudi Arabia*
[e] *Integrated Molecular Plant Physiology Research, Department of Biology, University of Antwerp, 2020, Antwerpen, Belgium*
[f] *Department of Zoology, Mar Ivanios College, Nalanchira, Thiruvananthapuram, India*

ARTICLE INFO

Keywords:
$ZnFe_2O_4/SnS_2$
Nanocomposite
Photocatalysis
Reusability

ABSTRACT

Binary p-n heterojunction of $ZnFe_2O_4/SnS_2$ nanocomposite (NCs) was constructed by sonochemical assisted for enhanced visible light induced photocatalytic performance. The narrow bandgap of 2.21 eV facilitated the photocatalyst be to active under visible-light irradiation. The rate of photodegradation of methylene blue (MB) dye by optimized-NCs ratio was observed to be remarkable with multifold enhancement than pristine $ZnFe_2O_4$ and SnS_2. The interfacial contact enforces an internal electric field dependent directional charge migration which hinders charge recombination that was verified by reduced photoluminescence intensity in NCs. Degradation process admits pseudo-first order kinetics. The scavengers assay predicts the major role of hydroxyl ($\cdot OH$) and superoxide ($\cdot O_2^-$) radicals in the degradation of MB dye. The structural stability and reusability of NCs were validated by six consecutive cycles experiment. This work provides guidance for rational design of heterojunction with superior activity and $ZnFe_2O_4/SnS_2$ NCs expressed a greater potential to be a photocatalyst to eliminate toxic pollutants from the aquatic resources.

1. Introduction

The recent advancement in nanotechnology encourages several modes of degradation yet photocatalysis is highly preferred because of its cost effective execution [1]. This utilizes photoelectrons to eliminate pollutants [2]. The presence of toxic dyes in the effluents might be life threatening as they are toxic carcinogen [3]. Hence, it is essential to remove hazardous materials present in the effluents. Recent urge for water resources, appreciates recycling and reusing water for the survival of living creatures.

In general, the association of metal cations in coordination with the oxygen atoms at the octahedral and tetrahedral positions which take up the spinel structure has a notation of AB_2O_4. Spinel ferrites are the metal oxides which hold dependency with the quantum, nature and site of occurrence of the metal cations in the crystal lattice [4]. They are widely applicable from drug delivery to photdegradation [5] *via* a catalyst. Their onset of action behind their role as a catalyst is to enhance the rate of chemical reaction. Owing to its catalytic role, they promote the reaction yield by undergoing physiochemical modifications. $ZnFe_2O_4$ are categorized under the normal ferrite which expresses least magnetic properties. On the other hand, when fabricated to nanometre scale their magnetic properties tend to enhance when magnetized [6]. The method, by which the ferrites are synthesized, also has an effect on the expression of magnetic properties [7]. The zinc ferrites are recognized due its magnetic applications [8], tetrahedral and octahedral sites are resided by the divalent Zn^{2+} and Fe^{3+} metal cations respectively. Though, these ferrites are applicable for electronic yet they are extended towards various innovative applications owing to its optical and magnetic properties. The magnetic moment of $ZnFe_2O_4$ has lead to its appreciable usage in biomedicine, sensors etc [8]. The zinc ferrites are

---

* Corresponding author.
E-mail address: sudheerkhan@bitsathy.ac.in (S.S. Khan).

https://doi.org/10.1016/j.matchemphys.2021.125464
Received 20 May 2021; Received in revised form 8 November 2021; Accepted 20 November 2021
0254-0584/© 2021

non-toxic to some extent and cost effective with abundant availability [9]. They are efficient photocatalyst in degrading the organic dyes that pollutes the environment [10].

Non-toxic SnS_2, a chalcogenide exhibits good visible light absorption with a band gap energy of 2.0–2.4 eV [11]. It is an n-type semiconductor with increased activity of catalysis. The limitation of SnS_2 in photocatalysis is the high rate of recombination of charge carriers, photo-corrosive effect and added to that it is unstable. Hence, it greatly affects its reusability [12]. Upon doping this narrow band gap semiconductor, it was reported to suppress the recombination of carriers [13]. This heterojunction creates an internal electric field that induces the release of the photogenerated charge carriers, hence suppresses the recombination [14].

Here, the current investigations harness the property of SnS_2 to make it suitable for visible light photocatalytic activity. Here, the nanohybrid was constructed with two materials, a p-type and an n-type semiconductor. Coupling of n-SnS_2 and *p*-$ZnFe_2O_4$ to fabricate p-n type interface will drive the migration of electron by the build-in electric field and thus could overcome the limitations of high recombination rate. In addition, considering that SnS_2 and $ZnFe_2O_4$ heterojunction would result in required band gap for visible light sensitization and enhanced stability. The novelty of this work is to design the method to boost the photocatalytic performance in a facile and less energy consumption manner. The hybrid material should possess better charge separation and high visible-light absorbing ability than the pristine individual parts. This study provides a perspective and guidance for the fabrication of efficient heterojunction for boosted photocatalysis. Thus, the study developed a novel n-SnS_2/p-$ZnFe_2O_4$ nanohybrid system and studied its photocatalytic activity under visible light illumination.

2. Materials and methods

2.1. Materials

Methylene blue (MB) dye, zinc sulphate heptahydrate ($ZnSO_4{\cdot}7H_2O$), ferrous sulphate ($FeSO_4$), stannous chloride ($SnCl_2$), silver nitrate ($AgNO_3$), *para*-benzoquinone and ethylenediaminetetraacetic acid (EDTA) were procured from Hi Media productions Ltd (Mumbai, India). tert-butyl alcohol was purchased from Sisco research laboratories, India. Sodium sulphide (Na_2S) was obtained from Nice chemicals, India. All the chemicals utilized here were of analytical grade.

2.2. Synthesis of $ZnFe_2O_4$

$ZnFe_2O_4$ was synthesized by simple chemical co-precipitation method. Here, 0.1 M of $ZnSO_4$ and 0.2 M of $FeSO_4$ were used as the precursors. The aqueous solution of 0.1 M $ZnSO_4$ was stirred vigorously with the addition of 0.2 M of $FeSO_4$ under persistent heat for about 30 min. Ammonia solution (25 mL) was added dropwise under heat for 30 min to achieve complete precipitation. The entire volume was kept for reflux at 100 °C for a span of 2 h. The precipitate was then washed twice with distilled H_2O and C_2H_5OH and dried at 90 °C. The obtained fine fraction was annealed at 500 °C for 1 h.

2.3. Formation of $ZnFe_2O_4$/SnS_2 NCs

The fabrication of $ZnFe_2O_4$/SnS_2 NCs was performed by sonochemical method. Here, 0.1 M of annealed $ZnFe_2O_4$ was dispersed in 100 ml of deionized water with an ultrasonic processor (Sonics, USA) for 30 min. Then the suspension was made by adding $SnCl_2$ and Na_2S in three different molar ratio (20, 40 and 60%) respectively. The suspensions were sonicated for 30 min. The entire volume obtained in three combinations of heterojunction was kept at reflux for 1 h. The precipitate was then washed twice with distilled H_2O and C_2H_5OH and dried at 90 °C. Pure SnS_2 was also synthesized with similar procedure as mentioned above without sonication and excluding $ZnFe_2O_4$.

2.4. Characterization of nanoparticles

In order to estimate the crystalline structure of $ZnFe_2O_4$/SnS_2 NCs, Powder X-Ray Diffraction (PXRD) was performed in 2θ range of 10–90° using the Cu-kα radiation ($\lambda = 1.54178$ A°) using Bruker D8 Advance [15]. Transmission electron microscopy (TEM) describes the morphology and their associated nanostructures (Jeol/JEM 2100). The chemical combinations of elements that exist in the NCs were determined with Energy dispersive X-ray spectroscopy (EDAX). Fourier transform infrared spectroscopy (FTIR) was done in Thermo Fisher scientific Nicolet IS50 to detect the chemical bond formation in the photocatalyst [16]. Brunauer-Emmett-Teller (BET) method detects the surface area of the photocatalyst which elicits N_2 sorption isotherm at 77.35 K using Quantachrome instruments, Autosorb IQ series. Chemical composition and the orientation of oxidation states in the decorated NCs were estimated by X-ray photoelectron spectroscopy (XPS) in Thermo Scientific™ ESCALAB™ Xi+ with monochromatized Al Kα excitation. UV–vis Diffusion Reflection Spectroscopy (UV–vis DRS) was carried out in PerkinElmer Lambda 750. The Raman spectroscopic technique was utilized to determine the vibrational modes of the molecule using WiTec alpha 300, Germany. The electrochemical impedance spectroscopy (EIS) was carried out in order to ensure the migration of e^-/h^+ using Metrohm Autolab Potentiostat (India). The photoluminescence spectra of SnS_2 decorated over $ZnFe_2O_4$ was determined using photoluminescence spectrophotometer (FLS 1000, Edinburgh Instruments).

2.5. Photocatalytic experiments

Photocatalytic potential of the fabricated $ZnFe_2O_4$/SnS_2 NCs was evaluated based on MB degradation with the generation of free radicals owing to the irradiation of visible light source. The samples are placed inside the experimental setup at a distance of 18.3 cm from the light source. Here, 3 mg/L of $ZnFe_2O_4$/SnS_2 NCs was dispersed in 20 mL of H_2O which was then infused into 25 mg/L of MB dye. The prepared test solution was kept under 500 W halogen lamp until visible degradation of MB dye happens. In order to obtain the degradation kinetics, the intensity of absorbance was measured subsequently for every 20 min. The quantity of MB dye residues in the test solution was determined by measuring the absorbance spectra in UV–visible spectrophotometer (Systronics, India) for every 20 min from 550 to 750 nm. The half-life ($t_{½}$) of MB by $ZnFe_2O_4$/SnS_2 NCs was found out from the plots of C/C_0 and 1-(C/C_0) versus time. Here, $t_{½}$ denotes half life of MB, C_0 and C were represented with their concentration of MB at initial time ($t = 0$) and at time t respectively. Owing to the rate at which the efficient degradation occurs in photocatalysis, their light-associated decomposition was reported by the expression,

$$-\ln\frac{C}{C_0} = kt \tag{1}$$

where k is the degradation rate constant (min^{-1}), C_0 and C are the concentration of MB at initial time ($t = 0$) and time t respectively. The percentage of MB degradation was determined using the formula mentioned below

$$\text{Degradation }(\%) = \frac{A_0 - A_t}{A_0} \times 100 \tag{2}$$

where A_0 denotes the initial absorption at $t = 0$ min and A_t denotes the absorption of MB solution at irradiation time (t). The photocatalysis of $ZnFe_2O_4$/SnS_2 NCs in three different molar ratios (20, 40 and 60%) were performed. In a similar way, photocatalysis of $ZnFe_2O_4$ and SnS_2 was also monitored separately by performing the same experiment.

This aids in better correlation and conclusion of efficient degradation of the desired photocatalyst. The experiment was further performed over different dosage of $ZnFe_2O_4/SnS_2$ NCs ranging from 1 to 5 mg/L to infer their corresponding modifications in the degradation efficiency.

Stability of $ZnFe_2O_4/SnS_2$ NCs is one of the limiting factors for their effective applications. Thus the potential to reuse the heterocatalyst was determined upon performing six cycles of experiments. In due course of time, $ZnFe_2O_4/SnS_2$ NCs were subjected to centrifugation, collected and they are re-dispersed in MB to validate the photocatalytic efficiency of recycled $ZnFe_2O_4/SnS_2$ NCs to degrade MB. XRD of the recovered $ZnFe_2O_4/SnS_2$ NCs were performed in order to investigate their structural stability and photo-corrosive nature during photocatalysis.

The generation reactive oxygen species (ROS) up on visible light exposure to $ZnFe_2O_4/SnS_2$ NCs was evaluated by the addition of radical scavengers namely silver nitrate, *para*-benzoquinone, EDTA, tert-butanol for the entrapment of electrons (e^-), superoxide radicals ($\cdot O_2^-$), holes (h^+) and hydroxyl radicals (·OH) respectively. An overall photocatalytic mechanism of the modified $ZnFe_2O_4/SnS_2$ NCs was elucidated with the results obtained based on photocatalytic performance. All the experimental studies were carried out in triplicate.

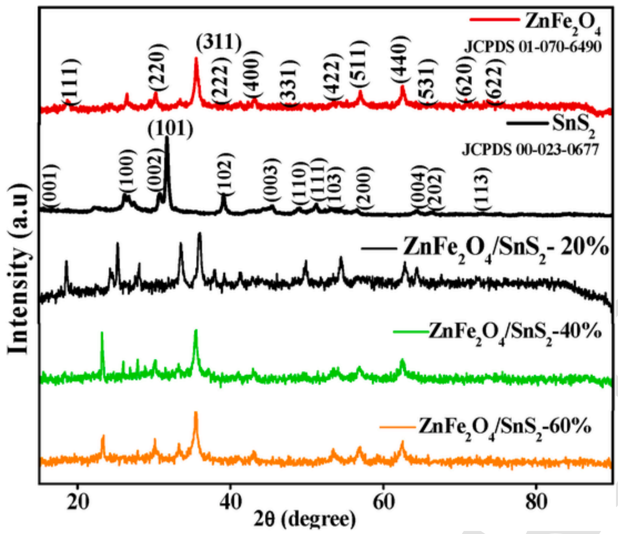

Fig. 1. Characterization of $ZnFe_2O_4/SnS_2$ NCs: XRD pattern.

3. Results and discussion

3.1. Characterization of $ZnFe_2O_4/SnS_2$ NCs

3.1.1. Structural studies

The crystal lattice and phase in $ZnFe_2O_4/SnS_2$ NCs, $ZnFe_2O_4$ and SnS_2 were established from Powder X-Ray diffraction studies. The diffractogram of $ZnFe_2O_4/SnS_2$ NCs were correlated with pure $ZnFe_2O_4$ and SnS_2 which is represented in Fig. 1. Resemblance of peaks positions in pure $ZnFe_2O_4$ and SnS_2 were observed in $ZnFe_2O_4/SnS_2$ NCs-20, 40 and 60. The diffraction peaks for spinel $ZnFe_2O_4$ was observed at 2θ of 18.60$^?$, 30.33$^?$, 35.51$^?$, 38.24$^?$, 43.09$^?$, 46.75$^?$, 53.61$^?$, 57.10$^?$, 62.74$^?$, 65.18$^?$, 70.97$^?$ and 74.17$^?$ and they are indexed as (111), (220), (311), (222), (400), (331), (422), (511), (440), (531), (620) and (622) respectively (JCPDS file no: #01-070-6490). The diffraction peaks agrees well with literature [17,18]. The characteristic diffraction peaks of SnS_2 was observed at 2θ of 15.75$^?$, 26.27$^?$, 30.68$^?$, 31.7$^?$, 39.26$^?$, 45.45$^?$, 49.11$^?$, 51.68$^?$, 53.82$^?$, 58.3$^?$, 59.7$^?$, 64.17$^?$, 67.37 and 70.87 and they are indexed to (001), (100), (002), (101), (102), (003), (110), (111), (103), (200), (112), (004), (202) and (113) respectively (JCPDS file no: #00-023-0677). All the detected peak positions reported in SnS_2 matches well with literature [19]. The XRD patterns showed distinct narrow peaks which represents the high crystallinity of $ZnFe_2O_4/SnS_2$ NCs. Thus, the detected peaks associated with pure $ZnFe_2O_4$ and SnS_2 were observed in the diffractogram of $ZnFe_2O_4/SnS_2$ NCs-20, 40 and 60 NCs which indicates the decoration of SnS_2 over $ZnFe_2O_4$. Moreover, in the NCs pattern of the sulfide/ferrite, the appearance of additional peaks might be due to the chemical interaction between them during the synthesis. As SnS_2 was added, a slight intrinsic phase transition in $ZnFe_2O_4$ might have occurred that results in peak splitting and shifts in the XRD pattern [20].

3.1.2. Microscopic analysis

The morphology and orientation of $ZnFe_2O_4/SnS_2$ NCs-60 was determined by TEM analysis and it is represented in Fig. 2a. The image admits that SnS_2 was embedded over sheet-like $ZnFe_2O_4$ in $ZnFe_2O_4/SnS_2$ NCs-60. It was found that SnS_2 was homogenous over the well dispersed $ZnFe_2O_4$ (Fig. 2a). Fig. 2a indicates the HR-TEM image of $ZnFe_2O_4/SnS_2$ NCs-60 and it was highly crystalline with the presence of clear lattice fringes. Fig. 2b shows that the two continuous lattice fringes having a d-spacing 0.27 nm and 0.36 nm. These interplanar distance attributes to

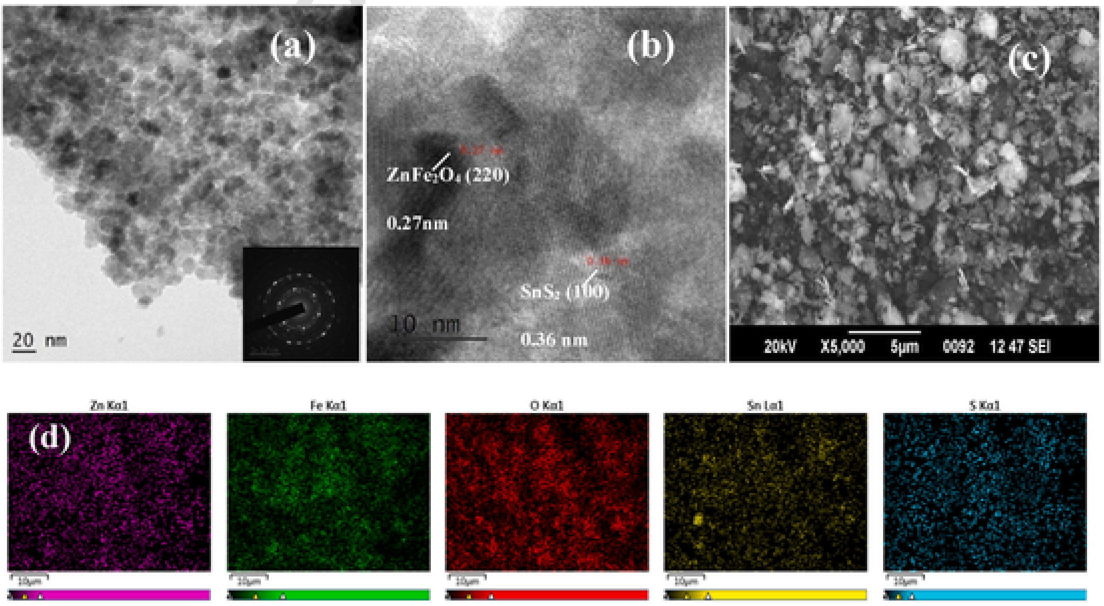

Fig. 2. (a) HR-TEM image, (a inset) SAED pattern, (b) HR-TEM with lattice fringes, (c) SEM image and (d) Elemental mapping.

(220) face of $ZnFe_2O_4$ and (100) face of SnS_2. These two distinct interplanar distances admits the formation of $ZnFe_2O_4/SnS_2$ NCs-60. The XRD data supported the d-spacing values of calculated NCs. The concept of making heterojunction between pure $ZnFe_2O_4$ and SnS_2 was observed with their well-defined contact and co-existence at their interfaces in the HR-TEM image. The selected area electron diffraction (SAED) pattern (Fig. 2a inset) ascribed the formation of ring which indicates the polycrystalline nature of $ZnFe_2O_4$ and SnS_2 in the fabricated $ZnFe_2O_4/SnS_2$ NCs-60. The particle size distribution of $ZnFe_2O_4/SnS_2$ NCs-60 ranged from 7.75 nm to 12.01 nm in the TEM image.

Morphology along with their nanostructures of the pure $ZnFe_2O_4$, SnS_2 and $ZnFe_2O_4/SnS_2$ NCs-60 were analysed in detail using SEM and EDAX. Fig. 2c depicts the morphology of $ZnFe_2O_4/SnS_2$ NCs-60. The SEM images of $ZnFe_2O_4$ and depicted in Supplementary Material Figs. S1a and b and it show the appearance of nanosheets and nanospheres respectively. Fig. 2d illustrates the elemental mapping of $ZnFe_2O_4/SnS_2$ NCs-60 and it admits the presence of Zn, Fe, O, Sn and S. EDAX analysis was carried out to ensure the elements that exist in the fabricated $ZnFe_2O_4/SnS_2$ NCs-60 (Supplementary Material Fig. S1c). After analysing, the elements were detected and distributed in their atomic % as follows Zn- 7.32%, Fe- 22.57%, O-59.44%, Sn-2.45% and S-8.22%.

3.1.3. Valence band state analysis

Chemical and electronic states of $ZnFe_2O_4/SnS_2$ NCs-60 and its individual counter parts $ZnFe_2O_4$ and SnS_2 were determined by XPS analysis. The survey spectrum along with their individual scan spectra were depicted in Fig. 3. In core-level Zn2p XPS spectra (Fig. 3b), two prominent peaks are noticed at binding energies of 1019.60 and 1043.6 eV for $Zn2p_{3/2}$ and $Zn2p_{1/2}$ respectively. The two peaks reported in the core-level Zn 2p XPS spectra was correlated and supported with the literature [21]. In the Fe 2p XPS spectra (Fig. 3c), two main peaks were centered at Fe $2p_{3/2}$ and Fe $2p_{1/2}$ with binding energies of 711.7 and

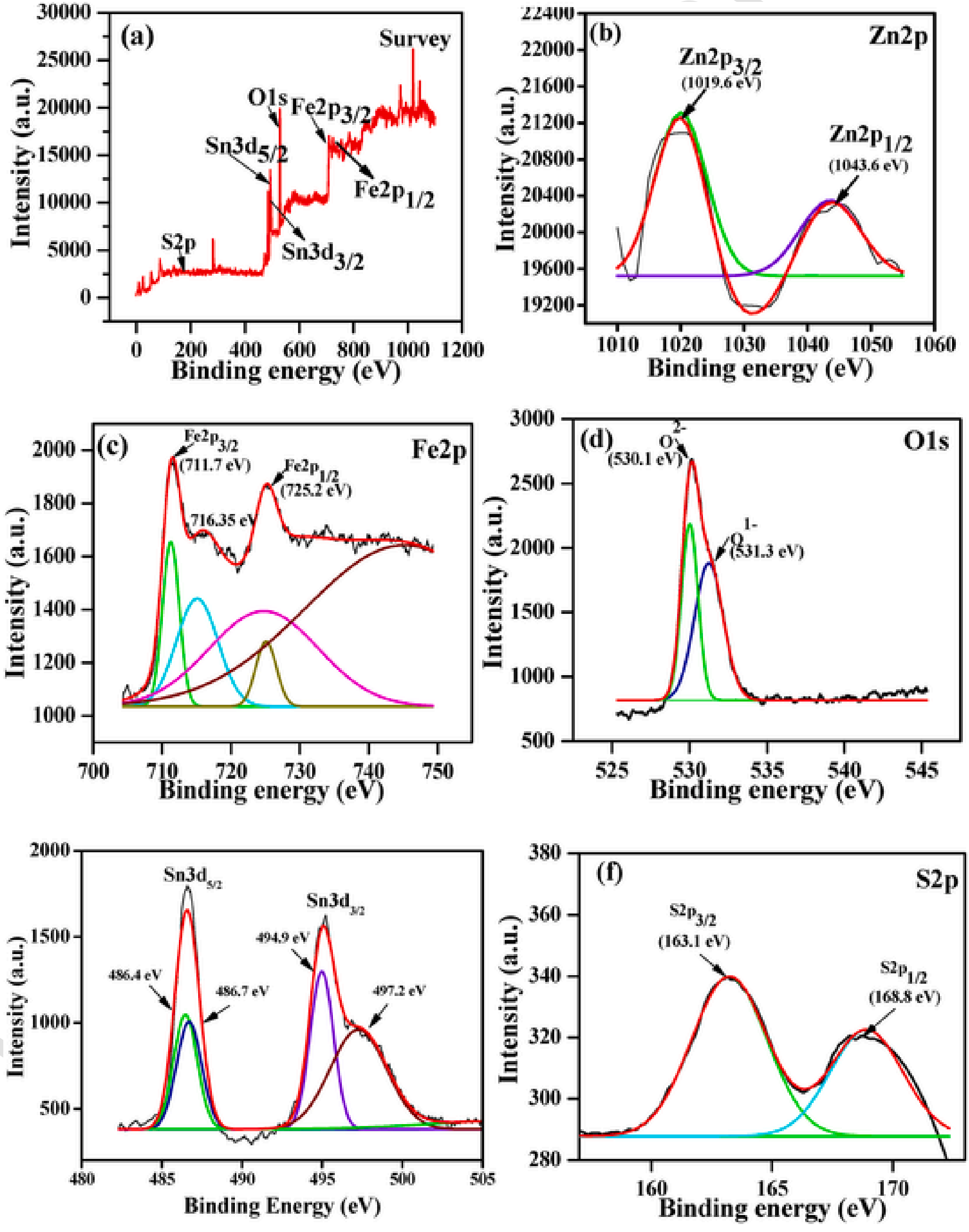

Fig. 3. XPS spectra of $ZnFe_2O_4/SnS_2$ NCs-60. (a) Survey spectra, (b) Zn2p scan, (c) Fe2p scan, (d) O1s scan, (e) Sn3d scan and (f) S2p scan.

725.2 eV respectively. The shake-up satellite peaks are located to the right side of the two peaks with a binding energy of 716.35 eV. The Fe 2p XPS spectrum matches well with study by Chen et al. [22]. The core-level O1s XPS spectrum (Fig. 3d) is found to be broad and asymmetric with the existence of multi-component O_2 species. In the O 1s XPS spectra, it can be deconvoluted by incorporating a curve-fitting procedure with two peaks of binding energies which are approximately 530.1 and 531.1 eV. The former is the inherent oxygen atoms that bound itself to metals such as Fe and Zn and the latter is the adsorbed oxygen [23]. According to Dupin et al. [24] the least binding energy peak is assigned to O^{2-} ionic state, the middle binding energy peak to O^{1-} ionic state and the highest binding energy peak is assigned to O_{chem} state (chemically absorbed oxygen). The O 1s XPS spectra were fitted at O^{2-} and O^{1-} states with the supporting data from the literature [24,25]. In Sn 3d XPS spectra, two peaks at 486.4 and 486.7 eV concurs with the binding energies of $Sn3d_{5/2}$ and 494.9 and 497.2 eV can be attributed to $Sn3d_{3/2}$ respectively can be seen in Fig. 3e [26]. Fig. 3f depicts the core level XPS spectra of S 2p, wherein the peaks at 163.1 and 168.8 eV are attributed to S $2p_{3/2}$ and S $2p_{1/2}$ respectively. These two symmetrical peaks admit that these two electronic states of S $2p_{3/2}$ and S $2p_{1/2}$ are the characteristics of S^{2-} in SnS_2 [27]. These results indicate that the $ZnFe_2O_4/SnS_2$ NCs has the major elements Zn, Fe, O, Sn and S, which agrees well with the results of XRD and EDAX. The XPS spectra of $ZnFe_2O_4$ and SnS_2 were depicted in Supplementary Material Figs. S2a and b. It is interesting to observe the peaks of Sn 3d in NCs materials are slightly shifted towards to higher binding energy relative to pure SnS_2 NPs. The XPS spectra that shows binding energy shifts is due to screening effect arising from the strong electronic interaction between two semiconductors. The heterojunction lead to electron migration from one to the other NPs to bring their Fermi levels equal. It leads ultimately to electron screening effect, thus contributing to a slight shift in the binding energies of constituent atoms [28].

3.1.4. Photoluminescence spectra

Migration of photogenerated charge carriers (e^-/h^+) and the capacity of the fabricated photocatalyst to transfer and entrap the emitted charge carriers can be evaluated by photoluminescence spectroscopy. The Photoluminescence spectra of $ZnFe_2O_4/SnS_2$ NCs were excited at 387 nm in room temperature. It was noticed that the intensity of photoluminescence emission spectra in the $ZnFe_2O_4/SnS_2$ NCs tend to be decreased in comparison with $ZnFe_2O_4$ and SnS_2 (Fig. 4a). This reduction in intensity has occurred as a result of quenching mechanism [29]. This data coincides with the consistent decrease in photoluminescence intensity of the NCs than the similar NPs spectra as reported in previous literatures [30–33]. Fewer tendencies of recombination of photogenerated charge carriers (e^-/h^+) in $ZnFe_2O_4/SnS_2$ NCs improvised their

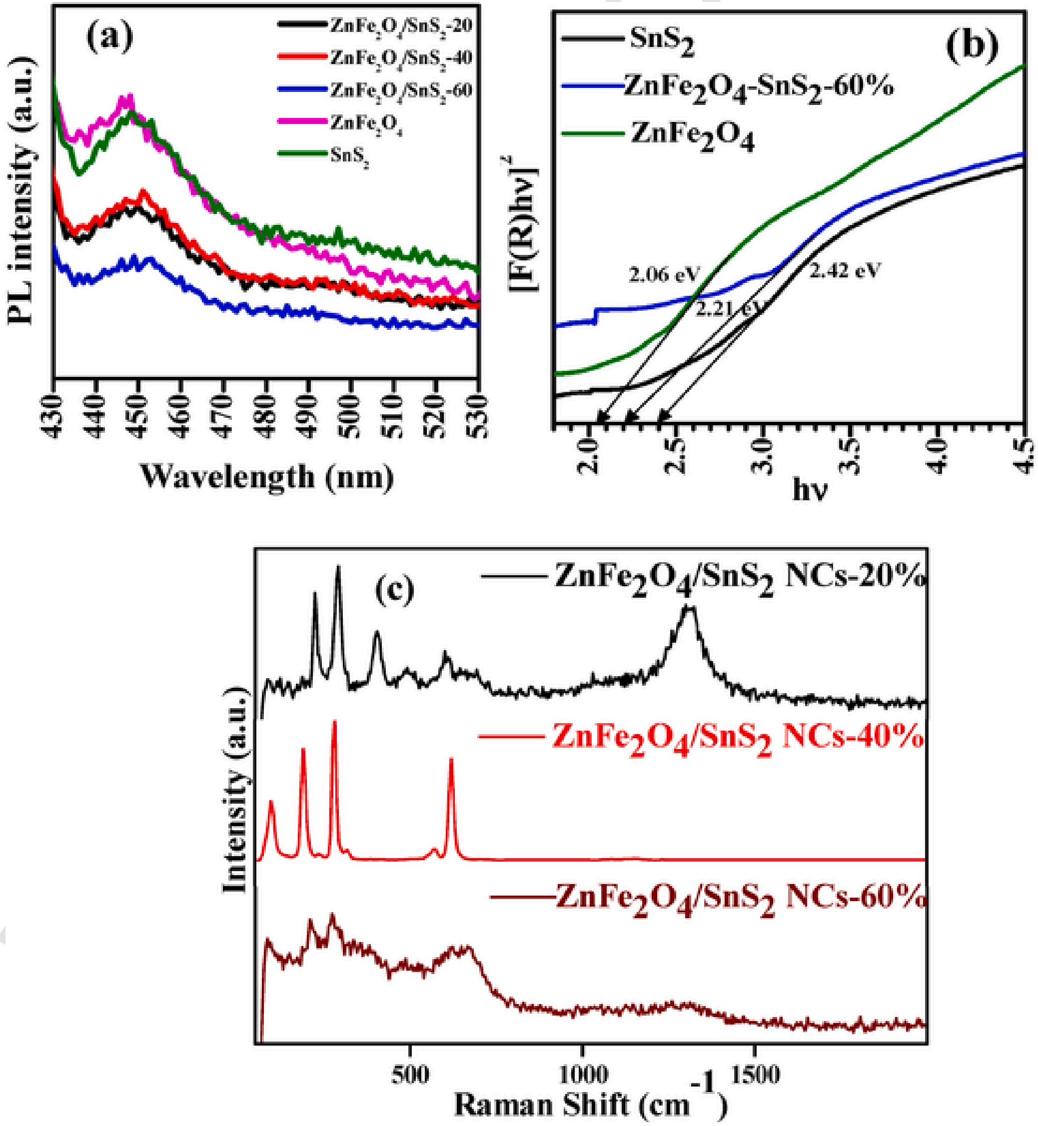

Fig. 4. (a) PL spectra (b) Kubelka-Munk plot of $ZnFe_2O_4/SnS_2$ NCs-60, SnS_2 and $ZnFe_2O_4$ and (c) Raman spectra of $ZnFe_2O_4/SnS_2$ NCs.

light-driven catalytic performance. The creation of defects enhances the crystalline structure of NCs [34].

A special terephthalic acid (TA) photoluminescence was employed to study the formation of ·OH radicals in photocatalysis experiment. Here, TA was used as a probe that generate PL spectra after interaction with ·OH radicals due to formation of 2-hydroxy terephalic acid. Similar photocatalytic experimental set-up was conducted keeping TA as a substrate. The PL spectrum was recorded after 180 min of irradiation of $ZnFe_2O_4/SnS_2$ NCs under visible light is represented in Supplementary Material Fig. S3a. The high intense PL intensity at 432 nm was observed that implies that the fluorescence resulted from TA and ·OH interactions. This confirms that ·OH is formed during the photocatalytic process [35–37].

3.1.5. *Photocurrent*

To ensure the activity of $ZnFe_2O_4/SnS_2$ NCs under visible light, transient photocurrent response of the NCs was measured. The better separation of charge carriers in $ZnFe_2O_4/SnS_2$ NCs than $ZnFe_2O_4$ and SnS_2 NPs was understood by the photocurrent response intensity. The NCs electrode was subjected to on-off cycles with photons radiation. The photocurrent of NCs indicates that when the light is in off cycle, the generated photocurrent reaches back to zero. This indicates the generation of photocurrent is owing to photoactive nature of $ZnFe_2O_4/SnS_2$ NCs. $ZnFe_2O_4/SnS_2$ NCs have highest transient photocurrent than $ZnFe_2O_4$ and SnS_2 indicates the better separation of charge carriers.

3.1.6. *Optical properties*

The UV–vis reflectance spectra of $ZnFe_2O_4/SnS_2$ NCs-60 with their individual counter parts SnS_2 and $ZnFe_2O_4$ is represented in Supplementary Material Fig. S3b. Enhanced light absorbing capacity increases the generation of photogenerated charge carriers manifold thereby improvising the photocatalytic performance of the prepared NCs. Plots between F(R) hv^2 and (hv) were performed from the following equation:

$$F(R)\ hv^2 = A\ (hv - E_g) \tag{3}$$

where, F(R), h, v, A and E_g represents the Kubelka-Munk function, Planck's constant, frequency of light, a constant and band gap energy respectively. Determination of band gap energy is done by extrapolating the linearity of the plot. The band gap of pure $ZnFe_2O_4$ and SnS_2 was validated to be 2.06 and 2.42 eV respectively. As a result of decorating SnS_2 over $ZnFe_2O_4$, the band gap energy was deviated to 2.21 eV for $ZnFe_2O_4/SnS_2$ NCs-60. Upon correlating the results obtained, it is confirmed that the fabrication of NCs aids in the utilization of light energy in the visible region. Hence, the investigation of photocatalysis was enhanced by the prepared NCs in the current study.

3.1.7. *Raman spectra*

Raman spectroscopic analysis was carried out for $ZnFe_2O_4/SnS_2$ NCs with its three different molar percentages - 20, 40 and 60 (Fig. 4c). Spinel $ZnFe_2O_4$ belong to the space group Fd3m [38] and their corresponding Raman spectra has five modes such as A_{1g}, E_g, $3F_{2g}$ [39]. This vibrational species has three Raman active modes (F_{2g}(1), F_{2g}(2) and F_{2g}(3)). However, the spectral intervals recorded between 600 and 800 cm^{-1} is the region of A_{1g} modes, 410-550 cm^{-1} is the region that corresponds to F_{2g}(3) modes and 260-380 cm^{-1} is responsible for the F_{2g}(2) modes. The vibrational modes of Eg and F_{2g}(1) were detected at low levels of frequencies [40]. The second order vibrational modes were observed at higher frequencies around 1000-1800 cm^{-1}. In Raman spectra of $ZnFe_2O_4/SnS_2$ NCs-20, the peaks observed at 602.38, 646.34, 661.94, 693.85, 730.01 and 793.12 cm^{-1} indicates the A_{1g} mode. Peaks at 223.72 and 291.8 cm^{-1} indicate F_{2g} (2) mode. The peaks at 406.67, 498.85 and 534.30 cm^{-1} symbolizes the F_{2g} (3) mode. The corresponding peaks of second order vibrational mode were recorded at 1032.8, 1171.78 and 1315.08 cm^{-1}. In the spectra of $ZnFe_2O_4/SnS_2$ NCs-40, the peaks observed at 248.25 cm^{-1} indicates F_{2g} (2) mode. The peaks at 434.9 and 470.76 cm^{-1} symbolizes the F_{2g}(3) mode. E_g and F_{2g} (1) modes are detected at low frequencies with the raman shift of 85.32, 153.34 and 221.89 cm^{-1}. Peaks that represent second order vibrational modes and A_{1g} mode were devoid in the Raman spectra of $ZnFe_2O_4/SnS_2$ NCs-40. In $ZnFe_2O_4/SnS_2$ NCs-60, the peaks recorded at 622.23, 649.89, 678.25 and 789.58 cm^{-1} represents A_{1g} mode. The vibrational mode of F_{2g}(3) was observed at 47.23, 479, 522 and 550.6 cm^{-1}. The Raman active mode F_{2g}(2) was recorded at peaks of 275.49, 323.70, 339.30, 354.90, 383.27 and 403.12 cm^{-1}. Peaks detected at lower frequencies such as 88.29, 147.85, 184.01 and 211.67 cm^{-1} indicates E_g and F_{2g}(1) vibrational modes. The second order vibrational modes were detected at 1028, 1163, 1255, 1346 and 1666 cm^{-1}. During the Raman-active vibrations, the dynamics in terms of normal modes inside the spinel unit cell are explained with respect to octahedral unit (AO_4) and tetrahedron unit (BO_6). The reason behind the peak in the region A_{1g} mode is recorded as the symmetric breathing of AO_4 unit occurred within the spinel lattice of $ZnFe_2O_4$ [41,42]. The low frequency Raman modes ascribe to the anti-symmetric breathing of tetrahedral unit (AO_4) and the vibrations in the octahedral sites (BO_6) [43]. The Raman active mode (Eg) is due to the symmetric bending motion of the anionic oxygen located within the AO_4 unit [44]. The least frequency F_{2g}(1) mode is attributed to the complete translation of the AO_4 within the spinel lattice [45]. The existence of F_{2g}(2) modes is due to the opposite motion of the oxygen atoms and cations along with the unidirectional motion of lattice [46]. Raman active F_{2g}(3) modes contributed to asymmetric bending motion of the oxygen atoms to the cations located at tetrahedral site [47]. The Raman spectrum of SnS_2 exhibits an intense peak at 323.70 cm^{-1} which attributes to the vibrational mode of A_{1g} mode. The peak indicates the out of plane stretching of sulphur atoms in SnS_2 [48,49]. The vibrational mode E_g represents the in-plane stretching of sulphur atoms in SnS_2 at 211.67 cm^{-1}. This particular vibrational mode is extremely weak owing to the effect of nanostructures. Since, nano-level size reduction is done, the possible scattering sites for in-plane scattering decreases and it causes weakening of E_g mode [50]. These two vibrational modes are detected only in the Raman spectra of $ZnFe_2O_4/SnS_2$ NCs-60 as the concentration of SnS_2 is higher when compared to $ZnFe_2O_4/SnS_2$ NCs-20 and 40. Thus, the Raman active modes of SnS_2 [51] and $ZnFe_2O_4$ [41] were confirmed in the prepared $ZnFe_2O_4/SnS_2$ NCs-60.

3.1.8. *Electrochemical impedance spectra*

Upon excitation of photons when irradiated under visible light, the photogenerated charge carriers are produced and they get migrated. The transfer of charges in the photocatalyst was confessed by EIS. Generally, the small arc radius explains the effectiveness of charge transfer and the lower charge resistance of the sample. The prepared $ZnFe_2O_4/SnS_2$ NCs-60 retains smaller arc radius than their individual counter parts $ZnFe_2O_4$ and SnS_2 (Supplementary Material Fig. S3c). The obtained result admits that the prepared NCs hold considerable migration of e^-/h^+. The separation of e^-/h^+ pair is well agreed with photoluminescence data.

3.1.9. *ESR analysis*

The reactive species involving in photocatalytic degradation process were identified further by using ESR (electron spin resonance) experiments (Supplementary Material Fig. S3d). The signal intensity of $ZnFe_2O_4/SnS_2$ NCs-60 for trapping $\cdot O_2^-$ free radical is stronger than $ZnFe_2O_4$ and SnS_2 NCs. These results suggest us that the amount of $\cdot O_2^-$ present in the system of $ZnFe_2O_4/SnS_2$ NCs-60 is more than that of SnS_2 after coupling $ZnFe_2O_4$. This may be attributed to the formation of heterojunction that resulted in better charge separation, making e^- more available to generate $\cdot O_2^-$ in NCs.

3.1.10. BET analysis

The profile of N_2 sorption isotherm is represented in Supplementary Material Fig. S3e. In accordance to the profiles of adsorption isotherm, the experimentally acquired data could empirically describe the multilayer adsorption isotherms by Brunauer- Emmett- Teller (BET) [52]. Owing to the saturation of nitrogen gas at the interfacial surface of NCs, the gas molecules clump together and forms multilayer adsorption. The porosity and specific surface area are taken into consideration while analysing adsorption, heterogenous catalysis and the associated reaction occur on the surface of the nanostructures. The significant role played by these two parameters decides the diffusion of charge carriers and its associated enhancement in light-driven catalytic activity. Owing to the porous structure, active sites are created at the interface of NCs to a larger extent [53]. The specific surface area of $ZnFe_2O_4/SnS_2$ NCs-60, pure $ZnFe_2O_4$ and SnS_2 were 141.21, 113.79 and 104.26 m^2/g respectively. It was comparatively higher for the decorated NCs. Higher surface area in NCs can enhance the degradation of MB dye by creating more vacant defects. The BJH desorption pore size distribution curves of $ZnFe_2O_4/SnS_2$ NCs-60 was recordd. The peak positions in isotherm curve admit that the mean pore diameter was 2.97 nm and it exhibits mesoporous nature. The profile of $ZnFe_2O_4/SnS_2$ NCs-60 admits that it follows Type IV adsorption isotherm [54], with a hysteresis loop. In addition to this, capillary condensation occurs in the mesopores. The former loop describes the multilayer adsorption and latter loop explains desorption. BJH pore size distribution in $ZnFe_2O_4/SnS_2$ NCs-60, SnS_2 and $ZnFe_2O_4$ was validated and tabulated in Table 1 which illustrates the size and volume of the pore.

3.2. Photocatalytic evaluation of $ZnFe_2O_4/SnS_2$

In order to validate the light-driven catalytic activity of $ZnFe_2O_4/SnS_2$ NCs, the degradation of MB owing to the incorporation of $ZnFe_2O_4/SnS_2$ NCs was estimated when irradiated under a visible light source. The spectra of UV–visible absorption depict a persistent reduction in the optical densities of MB dye over 180 min by $ZnFe_2O_4/SnS_2$ NCs-20, 40 and 60 (Fig. 5a). It took around 280 min in the presence of individual $ZnFe_2O_4$ and SnS_2. Methylene blue (MB) was opted to be a test pollutant. A limited quantity of test material can bringforth a striking difference since the dye is photo-oxidized [55].

Table 1
BET surface areas, pore volume and pore size values of the prepared samples.

Sample	Specific Surface area (m^2/g)	Average pore diameter (nm)	Pore volume (cm^3/g)
$ZnFe_2O_4$	113.79	2.48	0.076
SnS_2	104.26	2.22	0.048
$ZnFe_2O_4/SnS_2$-60	141.21	2.97	0.105

The reduction in λ_{max} of MB at 670 nm under visible light was due to the existence of chromogenic groups [56]. The evanishing of cationic MB dye was noted down in correspondence with the gradual reduction of absorbance at 670 nm. The plot between C_t/C_0 and 1-C_t/C_0 against time was utilized for the identification of half-life ($t_{1/2}$) of MB dye owing to the existence of $ZnFe_2O_4$, SnS_2, and $ZnFe_2O_4/SnS_2$ NCs- 20, 40 and 60. The convergence of the lines C_t/C_0 and 1-C_t/C_0 depicts half-life ($t_{1/2}$) of MB by the modified NCs which were 70, 50, 45, 110 and 160 min for $ZnFe_2O_4/SnS_2$ NCs-20 and 40 (Supplementary Material Figs. S4a and S4b), $ZnFe_2O_4/SnS_2$ NCs-60 (Fig. 5b), $ZnFe_2O_4$ and SnS_2 (Supplementary Material Figs. S4c and S4d) respectively. The $t_{1/2}$ of MB by the composite of $ZnFe_2O_4$ and SnS_2 was higher when compared with their individual ones.

Effectiveness of $ZnFe_2O_4/SnS_2$ NCs by light-driven catalysis was established upon correlating the degradation efficiency of $ZnFe_2O_4$, SnS_2 and $ZnFe_2O_4/SnS_2$ NCs-20, 40 and 60. Upon considering degradation efficiency and the half-life period of $ZnFe_2O_4/SnS_2$ NCs, it was noticed that the combined effect of $ZnFe_2O_4/SnS_2$ showed higher degradation than their individual parts $ZnFe_2O_4$ and SnS_2 separately. The complete degradation of MB by $ZnFe_2O_4/SnS_2$ NCs was confirmed with the UV–vis absorption spectrum at 670 nm within 240 min. Yet, based on the obtained half-life period of MB (45 min) by $ZnFe_2O_4/SnS_2$ NCs –60 (Fig. 5b), it was chosen to be the best outcome which is 3.25 times greater than SnS_2 and 2.6 times greater than $ZnFe_2O_4$ respectively. This confirms the formation of heterojunction owing to the suppression of recombination of photogenerated charge carriers (e^-/h^+).

Langmuir Hinshelwood (L-H) equation has a relation with the rate kinetics of dye degradation process by using photocatalyst, owing to the low concentration of MB [57].

The simplified form of L-H is

$$R = \frac{dC}{dt} = -kC \tag{4}$$

The integral of L-H equation gives:

$$Ln\,(C) = -kt + Ln\,(C_0) \tag{5}$$

where C_0 and k denotes initial absorption of MB at time (t = 0) and first order reaction constant. The plots between –ln (C_t/C_0) vs time was made to analyse the kinetics of degradation of MB over $ZnFe_2O_4/SnS_2$ NCs. The apparent degradation rate constant (k) of MB by $ZnFe_2O_4/SnS_2$ NCs was identified from Fig. 6(b). The k values for $ZnFe_2O_4/SnS_2$ NCs-20, 40 and 60 was 0.008, 0.013 and 0.013 min^{-1} respectively. Apparent degradation rate constant (k) and % of MB degradation $ZnFe_2O_4/SnS_2$ NCs- 40 and 60 was identical (Fig. 6c). The photocatalytic activity of the modified $ZnFe_2O_4/SnS_2$ NCs-60 was determined to be 91.78% which was comparatively higher than $ZnFe_2O_4/SnS_2$ NCs-20 (77.89%) and $ZnFe_2O_4/SnS_2$ NCs-40 (90.98%). It was inferred that absorption of light by photocatalyst happened, hence, the degradation

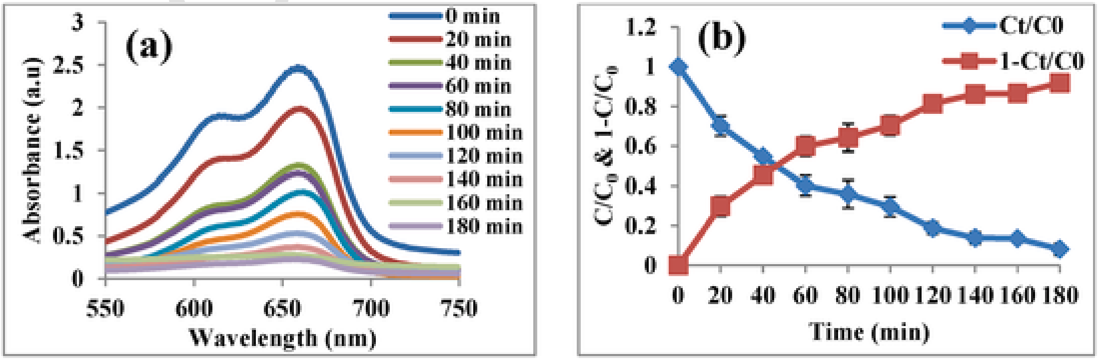

Fig. 5. (a) UV–vis absorption spectra of MB dye under visible light irradiation interaction with $ZnFe_2O_4/SnS_2$ NCs-60 and (b) the plot between C/C_0 and 1-C/C_0 versus time for $ZnFe_2O_4/SnS_2$ NCs-60.

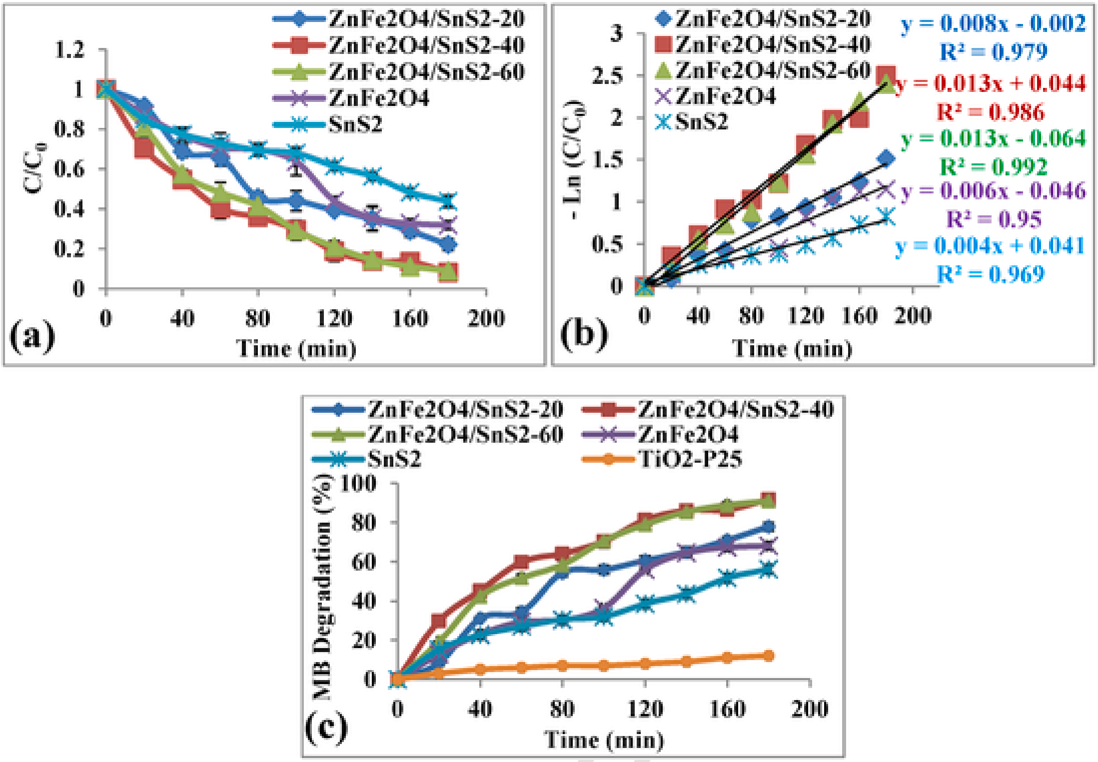

Fig. 6. (a) The plot between –Ln(C/C$_0$) and time, (b) The plot between C/C$_0$ and time, (c) degradation percentage of MB for ZnFe$_2$O$_4$/SnS$_2$ NCs-20, ZnFe$_2$O$_4$/SnS$_2$ NCs-40, ZnFe$_2$O$_4$/SnS$_2$ NCs-60, SnS$_2$ and ZnFe$_2$O$_4$.

of MB was achieved subsequently. The activity of the prepared photocatalyst was tested and compared with commercial TiO$_2$ P25 under visible light. TiO$_2$ P25 exhibited poor performance under visible light (since it is active only under UV light), whereas, ZnFe$_2$O$_4$/SnS$_2$ NCs-60 showed excellent activity (Fig. 6c). Further, the degradation of MB was poor presence of light without photocatalyst (photolysis) and in dark (with NCs) and it is represented Supplementary Material Fig. 4e. The results confirm the role of NCs under light irradiation to facilitate MB degradation.

The degradation kinetics was performed with five different doses (1–5 mg) of ZnFe$_2$O$_4$/SnS$_2$ NCs-60. The plot between C$_t$/C$_0$ and time at different dosage of ZnFe$_2$O$_4$/SnS$_2$ NCs-60 is represented in Fig. 7a. This illustrates that degradation efficiency elicits linearity with the dosage of ZnFe$_2$O$_4$/SnS$_2$ NCs-60. For an ideal photocatalyst, the initial degradation rate of NCs is highly dependable to concentration. This elicits the presence of more active sites in ZnFe$_2$O$_4$/SnS$_2$ NCs-60. Therefore, the dye degradation is achieved with more excitation of electrons [58].

Plot between -ln C$_t$/C and time was used to calculate first order rate constants in presence of different dosage of ZnFe$_2$O$_4$/SnS$_2$ NCs-60 (Fig. 7b). The results for 1–5 mg/L of NCs show high R^2 values (R^2 > 0.97). This ensures that data of the current experiment agrees well with Langmuir isotherm model [59]. This model exhibits equal affinity on ZnFe$_2$O$_4$/SnS$_2$ NCs-60 active sites with their ability to produce mononuclear coverage of MB molecules. The k value was found to be 0.008, 0.012, 0.009, 0.009 and 0.009 min^{-1} for 1–5 mg of NCs respectively (Fig. 7b). This shows that the degradation of MB dye by ZnFe$_2$O$_4$/SnS$_2$ NCs-60 occurred when irradiated under a visible light source.

3.3. *Scavenging study*

The phenomenal mechanism behind photocatalysis was explained by analyzing the performance of reactive species in the degradation process. This was analysed owing to the effect of scavengers with the modified ZnFe$_2$O$_4$/SnS$_2$ NCs-60. The incorporation of scavengers was to entrap the free radicals generated by the NCs due to visible light irradiation. In this study, AgNO$_3$, EDTA, tert-butanol and *para*-benzoquinone were utilized to entrap e$^-$, h$^+$, OH• radicals and $\cdot O_2^-$ radicals respectively. Free radical assay on MB degradation by NCs is shown in Fig. 8a.

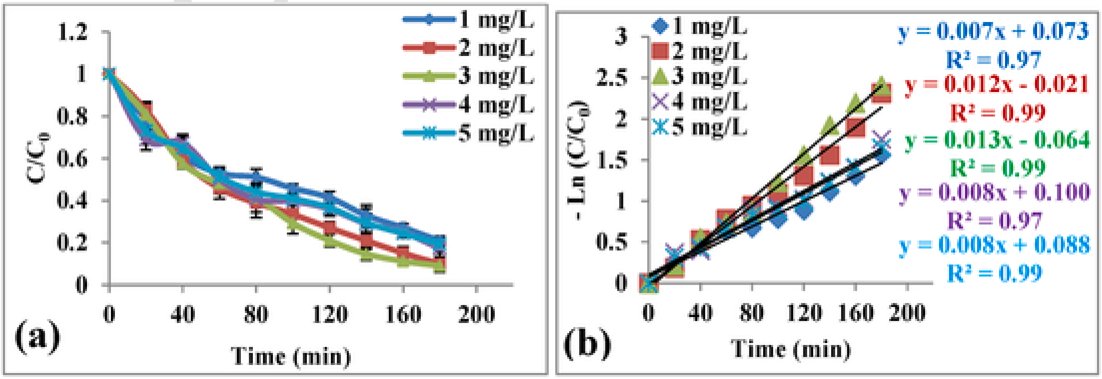

Fig. 7. (a) The plot between C/C$_0$ and time (b) The plot between –Ln (C/C$_0$) and time for different dosage of ZnFe$_2$O$_4$/SnS$_2$ NCs-60.

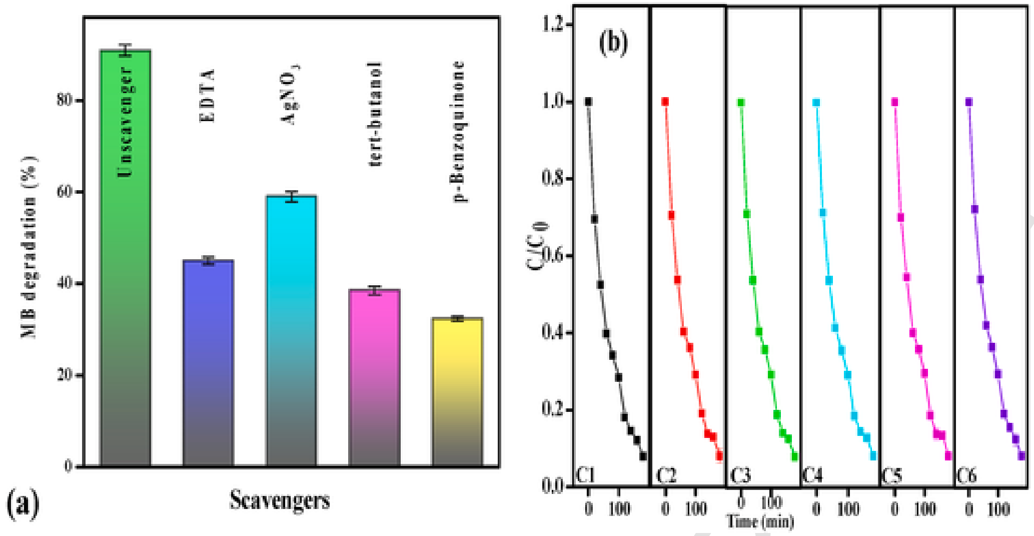

Fig. 8. (a) Free radical assay (b) Efficient reusability of $ZnFe_2O_4/SnS_2$ NCs-60.

Based on the scavenging result the major contribution in MB degradation was proved to be by OH• and $•O_2^-$. The results also suggest the role of e^- and h^+ in MB degradation. The role of OH• and $•O_2^-$ is verified by the TA photoluminescence and EIS respectively.

3.4. Reusability and structural stability

The most important criterion to behave as a photocatalyst is their stability throughout the degradation process. Similar protocols were utilized to perform subsequent cycle of experiments for recovered NCs. The percentage of MB degradation was estimated from the initial cycle till the 6th run of experiment. The percentage of MB degradation is depicted in Fig. 8b. Descriptive comparison done between published research works and the present study regarding photocatalytic activity of NCs and their efficiency to reuse is represented in Table 2. Chen et al. [60] studied and analysed the photocatalytic efficiency of In_2S_3/SnS_2 and attained photocatalytic activity of 55% and reusable efficiency of 87.27%. In present study, the reusable efficiency of $ZnFe_2O_4/SnS_2$ NCs-60 was determined to be 99.68% owing to the negligible difference in degradation during six consecutive cycles. The XRD studies were carried out for $ZnFe_2O_4/SnS_2$ NCs-60 after performing six consecutive cycles. The obtained diffractogram indicated the absence of new phase formation (Supplementary materials Fig. S4). The results indicated the structural stability of $ZnFe_2O_4/SnS_2$ NCs-60. This elucidated that the modified $ZnFe_2O_4/SnS_2$ NCs-60 is highly stable and suitable for reusing.

Table 2
Comparative data on photocatalysis of present work with available literature.

Authors	Particle	Photocatalytic activity (%)	Reusability (%) [Efficiency (%)]	References
Kuang et al.,	$ZnO/ZnFe_2O_4$	85.0	81.0 (95.20)	[59]
Chen et al.,	In_2S_3/SnS_2	55.0	48.0 (87.27)	[60]
Ahmadpour et al.,	TiO_2@ $ZnFe_2O_4/Pd$	86.1	71.3 (82.90)	[61]
Chen et al.,	Ni doped SnO_2/SnS_2	90.0	85.0 (94.44)	[62]
Dai et al.,	g-$C_3N_4/ZnS/SnS_2$	91.0	82.0 (90.10)	[63]
Akshhayya et al.,	$ZnFe_2O_4/SnS_2$ NCs −60	92.1	91.7 (99.68)	Present work

3.5. Mechanism of photocatalysis

The schematic depiction of light-driven catalytic mechanism of $ZnFe_2O_4/SnS_2$ NCs-60 is shown in Fig. 9. The deciding factors behind the mechanism of light-driven degradation indulge the following, the action of dye as an adsorbent over the surface of photocatalyst, the degradation achieved owing to the irradiation of light source alone and the degradation obtained by means of photocatalyst [61]. When the modified $ZnFe_2O_4/SnS_2$ NCs-60 were exposed to visible light source, the associated photogenerated charge carriers, e^- and h^+ were generated. This was the phenomenon beneath the photocatalysis of $ZnFe_2O_4/SnS_2$ NCs-60. The close interface formed between the NPs as seen in HRTEM, created a heterojunction and that could facilitate e^-/h^+ pair migration. The generated electron carriers upon reaction with an oxygen molecule bring forth the production of $·O_2^-$ radical . The generated holes upon reaction with an adsorbed H_2O formed hydroxyl group (-OH) to form OH• [62].

Upon interaction with the photons, the electrons at the surface get excited in the valence band. If the excitation energy is superior to the band gap, then corresponding excitation is absorbed in the conduction band too. The induction of photogenerated charge carriers was evaluated by calculating their corresponding E_{CB} and E_{VB} values. The calculated E_{CB} and E_{VB} of $ZnFe_2O_4$ are 0.18 eV and 2.24 eV respectively and on the other hand it is −0.34 eV and 2.08 eV for SnS_2 respectively. The heterojunction with p-n type semiconductors will result in enhanced charge carriers' separation. This is attributed to the driving force by interior electric field. The migration of e^-/h^+ pair from one photocatalytic system to other will help to reduce recombination rate. Before the hybridization of individual $ZnFe_2O_4$ and SnS_2 NPs, the separation of e^-/h^+ pairs is not facilitated owing to the nested band structure (Fig. 9). In n-type SnS_2, the fermi energy level (E_F) lies near CB and in p-type $ZnFe_2O_4$, the E_F lies near VB. While the construction of hybridization between SnS_2 and $ZnFe_2O_4$, the close contact results in formation of p-n heterojunction (Fig. 9) [63–66]. After hybridization, E_F of SnS_2 descends and E_F of $ZnFe_2O_4$ rose up until it reaches equilibrium in $ZnFe_2O_4$–SnS_2 nanohybrid. In this state, the inner electric field induces the region of SnS_2 to be positive charged and $ZnFe_2O_4$ to be negative charged. This results in the position of CB in SnS_2 to become more positive relative to $ZnFe_2O_4$. The e^- then moves towards the positive field and h^+ flows into the negative field, inducing charge carriers migration. The better separation was confirmed with respect to the observed photoluminescence and EIS spectra. Conversion of O_2 into ($·O_2^-$) superoxide radicals is possible since CB level of SnS_2 is more negative than the reduction potential of $O_2/·O_2^-$ (−0.33 eV) [67]. The VB level of

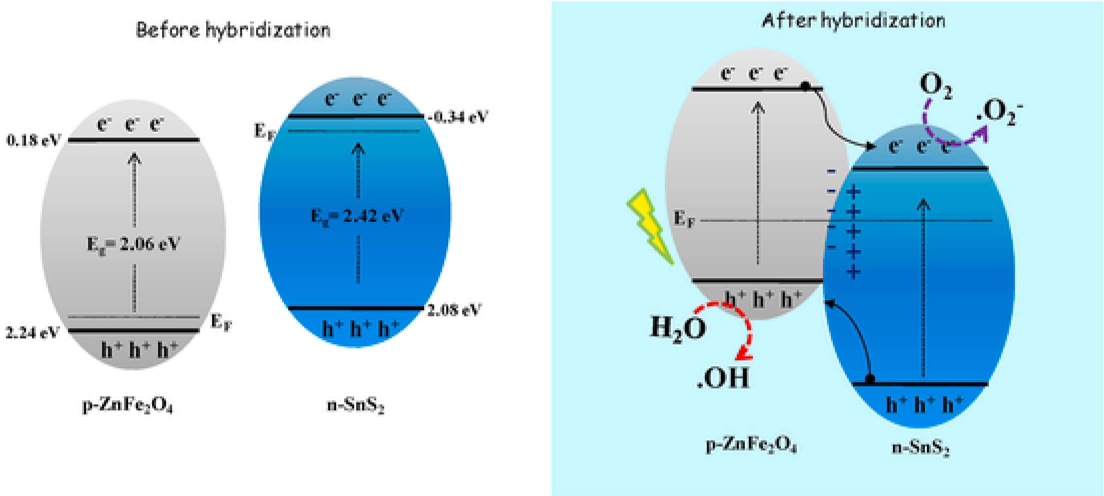

Fig. 9. Schematic depiction of light-driven catalytic mechanism of $ZnFe_2O_4/SnS_2$ NCs-60.

$ZnFe_2O_4$ is more positive than the reduction potential of $H_2O/{}^{\cdot}OH^-$ (1.99eV) [68] and so they elicit the ability to reduce H_2O to OH•. This was further ensured with the release of free radicals in accordance with the performance of scavengers, TA photoluminescence, and ESR. The generation of free radicals thus enhanced the photocatalytic mechanism. The holes in VB level of SnS_2 has a direct coordination with the MB and H_2O and emits hydroxyl radicals. Prime source of ROS to degrade MB was OH• and ${}^{\cdot}O_2^-$.

4. Conclusions

In conclusion, the investigations harness the potential of SnS_2 chalcogenide as a photocatalyst by construction of nano-heterojunction. Ultrasonic assisted co-precipitation method was used in the coupling of *p*-$ZnFe_2O_4$ and n-SnS_2. The interfacial contact results in p-n type heterojunction formation. $ZnFe_2O_4/SnS_2$ NCs-60 was optimized to show outstanding photocatalytic activity with the degradation efficiency of 91.70% in 45 min under visible light. The mechanism was elucidated by investigations of optical properties of NCs, electronic structures, scavenger assay, with combined experimental data and theoretical calculations. The p-n type interface prompted migration of electrons driven by internal electric field. The key ROS took part in photo-degradation of MB was OH• and •O_2^-. The NCs exhibited good reusability and resistance against photo-corrosion. Hence, the study suggests that $ZnFe_2O_4/SnS_2$ NCs-60 can be used as an efficient visible photocatalyst to eliminate hazardous pollutants from the water.

CRediT authorship contribution statement

C. Akshhayya: Methodology, Writing – original draft, Investigation, Formal analysis. **Mohammad K. Okla:** Writing – review & editing, Investigation, Funding acquisition, Formal analysis. **Ajith M. Thomas:** Investigation, Formal analysis. **Abdullah A. AL-ghamdi:** Investigation, Formal analysis. **Mostafa A. Abdel-Maksoud:** Investigation, Formal analysis. **Bander Almunqedhi:** Investigation, Formal analysis. **Hamada AbdElgawad:** Investigation, Formal analysis. **Lija L. Raju:** Investigation, Formal analysis. **S. Sudheer Khan:** Writing – review & editing, Funding acquisition, Supervision.

Declaration of competing interest

The authors declare that they have no known competing financial interests or personal relationships that could have appeared to influence the work reported in this paper.

Acknowledgement

The authors extend their appreciation to the Researchers Supporting Project number (RSP-2021/374) King Saud University, Riyadh, Saud Arabia. Authors thank the management of Bannari Amman Institute of Technology, Sathyamangalam, India for providing necessary facilities to carry out the work.

Appendix A. Supplementary data

Supplementary data to this article can be found online at https://doi.org/10.1016/j.matchemphys.2021.125464.

References

[1] K.N. Harish, H.S. Bhojya Naik, P.N. Prashanth kumar, R. Viswanath, Synthesis, enhanced optical and photocatalytic study of CD-Zn ferrites under sunlight, Catalysis Science & Technology 2 (2012) 1033–1039.
[2] Y.Y. Li, B.X. Zhou, H.W. Zhang, et al., Doping induced enhancement of crystallinity in polymeric carbon nitride nanosheets to improve their visible-light photocatalytic activity, Nanoscale 11 (2019) 6876–6885.
[3] J. Hu, L. Liua, Z. Xiao, Adsorptions of Cd (II) and methylene blue from aqueous solution by silica hybrid hollow spheres, RSC Adv. 5 (2015) 68092–68098.
[4] V. Kusigerski, V. Spasojevic, J. Magn, Magnetic properties and heating efficacy of magnesium doped magnetite nanoparticles obtained by co-precipitation method, J. Magn. Magn Mater. 475 (2019) 470–478.
[5] P.K. Boruah, M.R. Das, Ammonia-modified graphene sheets decorated with magnetic Fe3O4 nanoparticles for the photocatalytic and photo-Fenton degradation of phenolic compounds under sunlight irradiation, J. Hazard Mater. 325 (2017) 90–100.
[6] B.N. Sahu, R. Prabhu, N. Venkataramani, S. Prasad, R. Krishnan, A. Nabialek, O.M. Chumak, R. Zuberek, Magnetostriction studies in nanocrystalline zinc ferrite thin films by strain modulated ferromagnetic resonance, J. Magn. Magn Mater. 460 (2018) 203–206.
[7] S.J. Azhagushanmugam, N. Suriyanarayanan, R. Jayaprakash, Synthesis and characterization of nanocrystalline $Ni_{0.6}Zn_{0.4}Fe_2O_4$ spinel ferrite magnetic material, Physics Procedia 49 (2013) 44–48.
[8] M. Amiri, M. Salavati-Niasari, A. Akbari, Magnetic nanocarriers: evolution of spinel ferrites for medical applications, Adv. Colloid Interface Sci. 265 (2019) 29–44.
[9] M.S. Javed, Z. Jiang, Q. Yang, X. Wang, X. Han, C. Zhang, X. Gu, C. Hu, Exploring Li-ion hopping behaviour in zinc ferrite and promoting performance for flexible solid-state supercapacitor, Electrochim. Acta 295 (2019) 558–568.
[10] R. Rahimi, H. Kerdari, M. Rabbani, M. Shafiee, Synthesis, characterization and adsorbing properties of hollow ZnFe2O4 nanospheres on removal of Congo red from aqueous solution, Desalination 280 (2011) 412–418.
[11] X. Chen, J. Zhang, J. Zeng, Y. Shi, G. Huang, L. Zhang, H. Wang, Z. kong, J. Xi, Z. Ji, Novel heterojunction photocatalysts constructed by three-dimensional ln_2S_3 dandelions and ultrathin hexagonal SnS_2 nanosheets with excellent photocatalytic and photo electrochemical activities, Appl. Surf. Sci. 463 (2019) 693–703.
[12] D. Chen, S. Huang, R. Huang, Q. Zhang, T.T. Le, E. Cheng, R. Yue, Z. Hu, Z. Chen, Construction of Ni- doped SnO_2-SnS_2 heterojunctions with synergistic effect for enhanced photodegradation activity, J. Hazard Mater. 368 (2019) 204–213.
[13] Y.Y. Li, J.G. Wang, H.H. Sun, W. Hua, X.R. Liu, Heterostructured SnS_2/SnO_2

nanotubes with enhanced charge separation and excellent photocatalytic hydrogen production, Int. J. Hydrogen Energy 43 (2013) 14121–14129.

[14] J. Qu, D. Chen, N. Li, Q. Xu, H. Li, J. He, J. Lu, Coral-inspired nanoscale design of porous SnS_2 for photocatalytic reduction and removal of aqueous Cr (VI), Appl. Catal. B Environ. 207 (2017) 404–411.

[15] Z. Heidari, R. Alizadeh, A. Ebadi, N. Oturan, M.A. Oturan, Efficient photocatalytic degradation of furosemide by a novel sonoprecipitated ZnO over ion exchanged clinoptilolite nanorods, Separ. Purif. Technol. 4 (2020) 116800.

[16] X. Wang, J. Jian, Z. Yuan, J. Zeng, L. Zhang, T. Wang, H. Zhou, In situ loading of polyurethane/negative ion powder composite film with visible-light responsive Ag_3PO_4@AgBr particles for photocatalytic and antibacterial applications, Eur. Polym. J. 15 (2020) 109515.

[17] N. Zhang, S. Ruan, J. Han, Y. Yin, X. Li X, C. Liu, S. Adimi, S. Wen, Y. Xu, Oxygen vacancies dominated CuO@ $ZnFe_2O_4$ yolk-shell microspheres for robust and selective detection of xylene, Sensor. Actuator. B Chem. 295 (2019) 117–126.

[18] C. Zheng, C. Zhang, L. He, K. Zhang, J. Zhang, L. Jin, A.M. Asiri, K.A. Alamry, X. Chu, $ZnFe_2O_4$/ZnO nanosheets assembled microspheres for high performance trimethylamine gas sensing, J. Alloys Compd. 849 (2020) 156461.

[19] Qi Zhao, Hongpeng Zhang, Yi Liu, Mingming Zhu, Mingzhe Zhang, Magnetic and optical properties of two-dimensional SnS_2 nanosheets doped with Ho ions, Appl. Surf. Sci. 481 (2019) 1370–1376.

[20] R. Yassine, A.M. Abdallah, R. Awad, Z. Bitar, Structural, optical and magnetic properties of (x)NiO/(1-x)$CdFe_2O_4$ nanocomposites, Phys. B Condens. Matter 624 (2022) 413444.

[21] H.Y. Xu, Y.C. Liu, C.S. Xu, Y.X. Liu, C.L. Shao Cl, R. Mu, Room-temperature ferromagnetism in (Mn, N)-co doped ZnO thin films prepared by reactive magnetron co sputtering, Appl. Phys. Lett. 88 (2006) 242502.

[22] J. Chen, B. Zhu, Y. Sun, S. Yin, Z. Zhu, J. Li, Investigation of low-temperature selective catalytic reduction of NOx with ammonia over Mn-modified Fe_2O_3/AC catalysts, J. Braz. Chem. Soc. 29 (2018) 79–87.

[23] J. Liqiang J, W. Dejun, W. Baiqi, L. Shudan, X. Baifu, F. Honggang, S. Jiazhong, Effects of noble metal modification on surface oxygen composition, charge separation and photocatalytic activity of ZnO nanoparticles, J. Mol. Catal. Chem. 244 (2006) 193–200.

[24] J.C. Dupin, D. Gonbeau, P. Vinatier, A. Levasseur, Systematic XPS studies of metal oxides, hydroxides and peroxides, Phys. Chem. Chem. Phys. 6 (2000) 1319–1324.

[25] Z.Z: L.Q. Wu, Y.C. Li, S.Q. Li, Z.Z. Li, G.D. Tang, W.H. Qi, L.C. Xue, X.S. Ge, L.L. Ding, Method for estimating ionicities of oxides using O1s photoelectron spectra, AIP Adv. 24 (2015), 097210.

[26] S.C. Su, H.Y. Zhang, L.Z. Zhao, M. He, C.C. Ling, Band alignment of n-SnO_2/p-GaN hetero-junction studied by X-ray photoelectron spectroscopy, J. Phys. Appl. Phys. 47 (2014) 215102.

[27] L. Deng, Z. Zhu, L. Liu, H. Liu, Synthesis of Ag_2O and Ag co-modified flower-like SnS_2 composites with enhanced photocatalytic activity under solar light irradiation, Solid State Sci. 63 (2017) 76–83.

[28] M. Israr, J. Iqbal, A. Arshad, P. Gómez-Romero, Sheet-on-sheet like calcium ferrite and graphene nanoplatelets nanocomposite: a multifunctional nanocomposite for high-performance supercapacitor and visible light driven photocatalysis, J. Solid State Chem. 293 (2021) 121646.

[29] P.L. Reddy, K. Deshmukh, K. Chidambaram, M.M. Ali, K.K. Sadasivuni, Y.R. Kumar, R. Lakshmipathy, S.K. Pasha, Dielectric properties of polyvinyl alcohol (PVA) nanocomposites filled with green synthesized zinc sulphide (ZnS) nanoparticles, J. Mater. Sci. Mater. Electron. 5 (2019) 4676–4687.

[30] J. Sin, S. Lam, H. Zeng, H. Lin, H. Li, A.K. Kumaresan, A.R. Mohamed, J. Lim, Z-scheme heterojunction nanocomposite fabricated by decorating magnetic $MnFe_2O_4$ nanoparticles on BiOBr nanosheets for enhanced visible light photocatalytic degradation of 2,4-dichlorophenoxyacetic acid and Rhodamine B, Separ. Purif. Technol. 250 (2020) 117186.

[31] Z.H. Jaffari, S. Lam, J. Sin, H. Zeng, A.R. Mohamed, Magnetically recoverable Pd-loaded $BiFeO_3$ microcomposite with enhanced visible light photocatalytic performance for pollutant, bacterial and fungal elimination, Separ. Purif. Technol. 236 (2020) 116195.

[32] S. Lam, Z.H. Jaffari, J. Sin, H. Zeng, H. Lin, H. Li, A.R. Mohamed, D. Ng, Surface decorated coral-like magnetic BiFeO3 with Au nanoparticles for effective sunlight photodegradation of 2,4-D and E. coli inactivation, J. Mol. Liq. 326 (2021) 115372.

[33] J. Sin, S. Lam, H. Zeng, H. Lin, H. Li, K. Tham, A.R. Mohamed, J. Lim, Z. Qin, Magnetic $NiFe_2O_4$ nanoparticles decorated on N-doped BiOBr nanosheets for expeditious visible light photocatalytic phenol degradation and hexavalent chromium reduction via a Z-scheme heterojunction mechanism, Appl. Surf. Sci. 559 (2021) 149966.

[34] A. Kumar, L. Rout, L.S. Achary, S.K. Mohanty, P. Dash, A combustion synthesis route for magnetically separable graphene oxide–$CuFe_2O_4$–ZnO nanocomposites with enhanced solar light-mediated photocatalytic activity, New J. Chem. 41 (2017) 10568–10583.

[35] K.I. Ishibashi, A. Fujishima, T. Watanabe, K. Hashimoto, Detection of active oxidative species in TiO_2 photocatalysis using the fluorescence technique, Electrochem. Commun. 2 (2000) 207–210.

[36] W. Wang, X. Chen, G. Liu, Z. Shen, D. Xia, P.K. Wong, J.C. Yu, Monoclinic dibismuth tetraoxide: a new visible-light-driven photocatalyst for environmental remediation, Appl. Catal., B 176 (2015) 444–453.

[37] Jiajie Yu, Dongping Sun, Tianhe Wang, Feng Li, Fabrication of Ag@AgCl/ZnO submicron wire film catalyst on glass substrate with excellent visible light photocatalytic activity and reusability, Chem. Eng. J. 334 (2018) 225–236.

[38] V. D'Ippolito, G.B. Andreozzi, D. Bersani, P.P. Lottici, Raman fingerprint of chromate, aluminate and ferrite spinels, J. Raman Spectrosc. 46 (2015) 1255–1264.

[39] W.B. White, B.A. DeAngelis, Interpretation of the vibrational spectra of spinels, Spectrochim. Acta Part A Mol. Spectrosc. 23 (1967) 985–995.

[40] D.L. De Faria, S. Venâncio Silva, M.T. De Oliveira, Raman microspectroscopy of some iron oxides and oxyhydroxides, J. Raman Spectrosc. 28 (1997) 873–878.

[41] Shipra Choudhary, Aditi Bisht, Satyabrata Mohapatra, Microwave-assisted synthesis of α-Fe_2O_3/$ZnFe_2O_4$/ZnO ternary hybrid nanostructures for photocatalytic applications, Ceram. Int. 47 (2021) 3833–3841.

[42] D. Brian Hosterman, Raman Spectroscopic Study of Solid Solution Spinel Oxides, 2011.

[43] Z. Wang, D. Schiferl, Y. Zhao, H.S. O'Neill, High pressure Raman spectroscopy of spinel-type ferrite $ZnFe_2O_4$, J. Phys. Chem. Solid. 64 (2003) 2517–2523.

[44] T. Yamanaka, M. Ishii M, Raman scattering and lattice vibrations of Ni_2SiO_4 spinel at elevated temperature, Phys. Chem. Miner. 13 (1986) 156–160.

[45] C.M. Julien, M. Massot, Lattice vibrations of materials for lithium rechargeable batteries III lithium manganese oxides, Mater. Sci. Eng., B 100 (2003) 69–78.

[46] J.L. Verble, Temperature-dependent light-scattering studies of the Verwey transition and electronic disorder in magnetite, Phys. Rev. B 9 (1974) 5236.

[47] V. Sánchez Escribano, E. Fernández López, M. Panizza, C. Resini, J.M. Gallardo Amores, G. Busca, Characterization of cubic ceria–zirconia powders by X-ray diffraction and vibrational and electronic spectroscopy, Solid State Sci. 5 (2003) 1369–1376.

[48] A.J. Smith, P.E. Meek, W.Y. Liang, Raman scattering studies of SnS_2 and $SnSe_2$, J. Phys. C Solid State Phys. 10 (1977) 1321.

[49] Z. Wang, F. Pang, In-plane growth of large ultra-thin SnS_2 nanosheets by tellurium-assisted chemical vapor deposition, RSC Adv. 7 (2017) 29080–29087.

[50] H. Xiao, Y.C. Zhang, H. Bai, Molten salt synthesis of SnS_2 microplate particles, Mater. Lett. 63 (2009) 809–811.

[51] A. Joseph, C.R. Anjitha, A. Aravind, P.M. Aneesh, Structural, optical and magnetic properties of SnS_2 nanoparticles and photo response characteristics of p-Si/n-SnS_2 heterojunction diode, Appl. Surf. Sci. 528 (2020) 146977.

[52] M. Peleg, Assessment of a semi-empirical four parameter general model for sigmoid moisture sorption isotherms, J. Food Process. Eng. 16 (1993) 21–37.

[53] Z. Zhao, Y. Wang, J. Xu, C. Shang, Y. Wang, AgCl-loaded mesoporous anatase TiO_2 with large specific surface area for enhancing photocatalysis, Appl. Surf. Sci. 351 (2015) 416–424.

[54] M. Thommes, K. Kaneko, A.V. Neimark, J.P. Olivier, F. Rodriguez-Reinoso, J. Rouquerol, K.S. Sing, Physisorption of gases, with special reference to the evaluation of surface area and pore size distribution, Pure Appl. Chem. 87 (2015) 1051–1069.

[55] A. Mills, An overview of the methylene blue ISO test for assessing the activities of photocatalytic films, Appl. Catal. B Environ. 128 (2012) 144–149.

[56] Y.B. Kim, D. Cho, W.H. Park, Fabrication and characterization of TiO2/poly (dimethyl siloxane) composite fibres with thermal and mechanical stability, J. Appl. Polym. Sci. 116 (2010) 449–454.

[57] S.K. Mohapatra, N. Kondamudi, S. Banerjee, M. Misra, Functionalization of self organized TiO_2 nanotubes with Pd nanoparticles for photocatalytic decomposition of dyes under solar light illumination, Langmuir 24 (2008) 11276–11281.

[58] N. Wang, X. Li, Y. Wang, Y. Shang, X. Zhuang, H. Li, Z. Zhou, Combined process of visible light irradiation photocatalysis-coagulation enhances natural organic matter removal: optimization of influencing factors and mechanism, Chem. Eng. J. 374 (2019) 748–759.

[59] B. Janani, S. Swetha, Asad Syed, Abdallah M. Elgorban, Nouf S.S. Zaghloul, Ajith M. Thomas, Lija L. Raju, S. Sudheer Khan, Spinel FeV_2O_4 coupling on nanocube-like Bi_2O_3 for high performance white light photocatalysis and antibacterial applications, J. Alloys Compd. 887 (2021) 161432.

[60] X. Chen, J. Zhang, J. Zeng, Y. Shi, G. Huang, L. Zhang, H. Wang, Z. Kong, J. Xi, Z. Ji, Novel 3D/2D heterojunction photocatalysts constructed by three-dimensional In_2S_3 dandelions and ultrathin hexagonal SnS_2 nanosheets with excellent photocatalytic and photo electrochemical activities, Appl. Surf. Sci. 463 (2019) 693–703.

[61] J.J. Chen, J.C. Wu, P.C. Wu, D.P. Tsai, Improved photocatalytic activity of shell-isolated plasmonic photocatalyst Au@SiO_2/TiO_2 by promoted LSPR, J. Phys. Chem. C 116 (2012) 26535–26542.

[62] H.R. Rajabi, O. Khani, M. Shamsipur, V. Vatanpour, High-performance pure and Fe^{3+} ion doped ZnS quantum dots as green nanophotocatalysts for the removal of malachite green under UV-light irradiation, J. Hazard Mater. 250 (2013) 370–380.

[63] Zongjun Dong, Jiaqi Pan, Beibei Wang, Ziyuan Jiang, Chuang Zhao, Jingjing Wang, Changsheng Song, Yingying Zheng, Can Cui, Chaorong Li, the p-n-type Bi_5O_7I-modified porous C_3N_4 nano-heterojunction for enhanced visible light photocatalysis, J. Alloys Compd. 747 (2018) 788–795.

[64] Qin Geng, Hongtao Xie, He Ye, Yanjuan Sun, Xifeng Hou, Zhiming Wang, Dong Fan, Atomic interfacial structure and charge transfer mechanism on in-situ formed BiOI/$Bi_2O_2SO_4$ p–n heterojunctions with highly promoted photocatalysis, Appl. Catal. B Environ. 297 (2021) 120492.

[65] Shicheng Jia, Yuanting Feng, Haitao Zhang, Dongmei Jiang, Qingfeng Zhan, Interface engineered fabrication of Bi_4O_7/BiOCl 1D/2D p-n heterojunction for enhanced visible light driven photocatalysis, Opt. Mater. 109 (2020) 110174.

[66] F. Guo, W. Shi, H. Wang, M. Han, H. Li, H. Huang, Y. Liu, Z. Kang, Facile fabrication of a CoO/g-C_3N_4 p–n heterojunction with enhanced photocatalytic activity and stability for tetracycline degradation under visible light, Catalysis Science & Technology 7 (2017) 3325–3331.

[67] Q. Geng, H. Xie, Y. He, Y. Sun, X. Hou, W. Zhiming, F. Dong, Atomic interfacial structure and charge transfer mechanism on in-situ formed BiOI/$Bi_2O_2SO_4$ p–n heterojunctions with highly promoted photocatalysis, Appl. Catal. B Environ. 297 (2021) 120492.

[68] S. Xia, G. Zhang, Y. Meng, C. Yang, Z. Ni, J. Hu, Kinetic and mechanistic analysis for the photodegradation of gaseous formaldehyde by core-shell CeO_2@ LDHs, Appl. Catal. B Environ. 278 (2020) 119266–119278.